NIH Public Access
Author Manuscript
J Orthop Res. Author manuscript; available in PMC 2010 August 31.

Published in final edited form as:
J Orthop Res. 2010 June ; 28(6): 805–811. doi:10.1002/jor.21049.

An in-situ fluorescence-based optical extensometry system for imaging mechanically loaded bone

Christopher Price[1], **Wen Li**[1], **John E. Novotny**[1], and **Liyun Wang**[1]

[1]Center for Biomedical Engineering Research, Department of Mechanical Engineering, University of Delaware, Newark, Delaware, USA

Abstract

The application and quantification of well-controlled tissue strains is required for quantitative investigations into mechanisms of tissue adaptation within the musculoskeletal system. Although there are many commercial and custom extensometry systems for large biological samples, integrated loading/strain measurement for small samples are not as readily available. Advanced imaging modules such as laser scanning microscopy provide *in situ*, minimally invasive tools to probe cellular and molecular processes with high spatiotemporal resolution. Currently, there is a need to devise loading/strain measurement systems that can be integrated with such advanced imaging modules. In this paper we describe the development and validation of a fluorescence-based, optical extensometry system directly integrated within a confocal microscopy platform. This system will allow in-situ measurement of surface strain that is compatible with the direct imaging of cellular processes within small bone samples. This optical extensometry system is capable of accurately and reproducibly measuring physiologically relevant surface strains (200-3000 micro-strain) in beams machined from various well-characterized materials, including bovine femoral cortex, and in intact murine tibia. This simple optical extensometry system provides a powerful tool to further our investigation of the relationships between mechanical loading, fluid and solute transport, and mechanosensation within the musculoskeletal system.

Keywords

mechanical loading; digital image correlation; strain measurement; confocal microscopy; fluid flow

Introduction

Mechanical loading is a crucial factor influencing the growth and adaptation of the tissues of the musculoskeletal system, including bone, cartilage, muscle, tendon, and ligaments (1–3). Identification of the cellular mechanisms involved in sensing and adapting to mechanical load is actively pursued in current musculoskeletal research. In bone it has been hypothesized that tissue adaptation is initiated by osteocytes, the presumed “mechanosensors” embedded in the bone matrix, which sense and respond to changes in their mechanical environment (4,5). Osteocytes are thought to sense their mechanical environment indirectly through the load-induced fluid flows in the lacunar-cannicular system (4,5). Therefore, quantifying the effect of tissue strain on load-induced fluid flow is of significant importance in the study of bone mechanobiology. To this extent, our group recently published a modeling study indicating the feasibility of quantifying fluid/solute transport within intact loaded murine tibia using the

Address correspondence to: Liyun Wang, Center for Biomedical Engineering Research, Department of Mechanical Engineering, 130 Academy Street, Newark, DE 19716, Tel: 302-831-2659, Fax: 302-831-3619, lywang@udel.edu.

NIH-PA Author Manuscript
NIH-PA Author Manuscript
NIH-PA Author Manuscript

NIH-PA Author Manuscript

NIH-PA Author Manuscript

NIH-PA Author Manuscript

technique of fluorescence recovery after photobleaching (FRAP) (6,7). This study predicted that interstitial solute transport could be enhanced through the application of cyclic compressive loads, and the transport rate varied with the magnitude and frequency of the applied uni-axial load (strain). To confirm these predictions, fluid and solute transport needs to be directly quantified while the bone is subjected to well-controlled strains. Such studies require the development of an integrated system that allows i) applying and quantifying mechanical strains at specified regions of the murine tibia and ii) imaging of solute transport at the same regions. The challenge of imaging solute transport inside mineralized bone has been overcome by use of the FRAP approach and the optical sectioning capability of confocal microscopy (6,8) as demonstrated in studies performed on mouse tibiae devoid of mechanical loading. The present study aimed to incorporate the capability of load application and tissue strain quantification into a confocal imaging platform allowing future studies of fluid and solute transport in loaded bone.

Typically, tissue strains in bone have been quantified via strain gauges and extensometers, or analytically using mathematical modeling (9–12). However, these experimental techniques are not easily applied to small, irregular, or fragile bone samples (13) especially when subsequent live imaging will be performed on the samples. For example, repeatable placement and bonding of strain gauges is often difficult on small bones such as the mouse tibia. Possible tissue damage due to gauge bonding and removal precludes their use in experiments where transport imaging is also required within the measured region. Contact extensometry is less invasive but its accuracy is strongly influenced by device orientation relative to the principle strain direction and is confounded by small sample size, complex sample morphology, and device interaction with soft tissue. The accuracy of indirect, model-based strain measurement techniques is highly dependent on model complexity (including geometry, boundary conditions, material properties, and choice of constitutive model) and accurate location-specific strain measures often require intensive imaging and post-processing procedures (14). Because of the limitations of these conventional methods, a faster, less-invasive, and *in-situ/in-vivo* compatible technique for measuring strain on small irregular specimens is sought, especially for studies in which mechanical loading, strain measurement, and tissue imaging are to be integrated.

A promising technique for measuring surface strain in small samples is non-contact optical extensometry (15). Such systems are used extensively in material sciences and have been applied to the measurement of strain in a large number of biological tissues (13,16–19). In this paper, we describe the development and validation of an integrated *in-situ* loading and non-contact, non-destructive, fluorescence microscopy-based strain measurement system for small bone specimens. As tested the system is capable of accurately measuring physiologically relevant uniaxial surface strains in the range of 200 to 3000-με over gauge lengths up to 3.0-mm in beams machined from well-characterized materials as well as in intact irregularly shaped murine tibiae. By integrating widely used laser scanning microscopy and electromagnetic testing equipment the current strain measurement approach can also be combined with tools for imaging bone responses, such as fluid and solute movement among cells (6), to the application of well-defined mechanical loads (strains). Such studies are expected to yield valuable insights into the mechanisms of bone's mechanical adaptation.

Methods

Non-Contact Optical Strain Measurement System

The non-contact, optical extensometry device tested consisted of a material testing system integrated with a laser-scanning microscope (Figure 1a). The loading device consisted of an electromagnetic linear actuator (Electroforce LM1 Test Bench, Bose Corporation, Eden Prairie, MN) with a stroke length of ±6.5-mm (accuracy 0.002-mm), a 10-N load cell (accuracy

NIH-PA Author Manuscript

NIH-PA Author Manuscript

NIH-PA Author Manuscript

0.01-N), a reaction bracket, and a water bath. The device could be translated and titled to align the loading and imaging axes.

An inverted microscope (AxioObserver, Carl Zeiss Inc., Thornwood, NY) equipped with a laser scanning confocal module (LSM 510), epi-fluorescent UV illuminator (HBO 100, Carl Zeiss, Inc), and an externally attached digital camera (MRc5, Carl Zeiss Inc.) was used for optical strain measurements (Figure 1a). An objective inverter (LSM Technologies, Etters, PA) was used to direct the imaging path away from the inverted microscope stage and onto the mechanically loaded specimen (Figure 1a). Because the inverter optics is designed for fluorescence (not bright-field) imaging, fluorescent beads were used as markers of surface deformation (detailed below). Confocal imaging of the fluorescent beads on mechanically loaded samples was tested in preliminary studies. However, the pixel-by-pixel raster scanning pattern of the LSM 510 resulted in a relatively slow capturing speed (>4-sec/frame), which was found to be inadequate in preventing measurement errors due to small vibrations associated with the attached lens inverter and the bench-top electromagnetic motor. We thus chose to use an external CCD camera with a faster capture speed (~0.10 to 0.25-sec/frame) attached to the side port of the inverted microscope. Although the camera only detected epi-fluorescence signals and limited the strain measurements to the sample surface, the advantages of faster capture speed eliminated measurement errors due to motion artifacts and thus increased measurement accuracy.

Surface strain was determined by tracking fluorescent landmarks (patterns) on various materials (see below) during the application of specified loads. Fluorescent 10-micron spheres (Yellow-Green FluoSpheres, 495/510-nm absorption/emission, Invitrogen, Carlsbad, CA) were spread (~1.0-mL, or 3600 individual spheres) on the imaging surface and adhered to the specimen surface by evaporation before testing (Figure 1b). Plastic samples were tested dry. For bovine and murine bone samples micro-sphere application and strain testing were performed in a humidity chamber to prevent specimen dehydration. Humidity did not inhibit the adherence of the micro-spheres to bone. Once adhered micro-spheres could not be dislodged by wetting or flushing with PBS, remaining fixed to the surface during the tests. The attached spheres could be only removed by physically wiping them away.

All specimens were held within the testing system using custom loading grips. An initial compressive load of 2-N was applied for 10 sec to eliminate gaps and slippage among the loading fixtures and specimens. The load was then reduced to a baseline tar load of 0.2-N for 5–10 minutes prior to testing. During this period, the loading device was adjusted so that a flat, labeled region of the specimen surface was both in focus and inline with the imaging and loading axes. The specimens were then incrementally loaded to the levels specified below. At each specified load ten images (2584 × 500-pixels) were captured using the CCD camera (sequential frame rate = ~2-frames/sec). Use of a 2.5x objective corrected for field-flatness (EC-Epiplan-NEOFLUR, Carl Zeiss, Inc.) resulted in a resolution of 1.26-mm/pixel and a maximal image width in the direction of loading (i.e. gauge length) of ~3.2-mm. During image acquisition applied load was held static (10–15 sec). Load was increased between levels at 0.5-N/sec with a ramping duration of 1–2-sec.

Strain was quantified by determining load-induced deformation between manually chosen fluorescent patterns (Figure 1b) using a semi-automated digital image correlation (DIC) algorithm (IMAQ Vision Builder, National Instruments, Austin, TX). Briefly, unique patterns of micro-spheres were selected near the two margins of the baseline image. A rectangular bounding box, 100-by-200 pixels, was chosen to enclose each pattern of interest. Patterns were chosen so that they were aligned in the direction of the applied load, did not exit the field of view (FOV) during the test, maximized the initial inter-pattern gauge length (L_o), and resulted in a single correlation match. Using a normalized cross-correlation routine the IMAQ Vision

NIH-PA Author Manuscript

NIH-PA Author Manuscript

NIH-PA Author Manuscript

software searched images of the specimen at the different load levels, uniquely identified the selected patterns, and recorded their locations and inter-pattern distances (L) with sub-pixel accuracy (15,19) (Figure 1b). Uni-axial engineering strains were calculated as $\varepsilon = (L - L_o) / L_o$.

Optical Strain System Calibration

Several standard calibration procedures were performed to quantify potential strain error due to optical distortions such as spherical aberration and movement out of focus, and to quantify the accuracy of large and small strain measurements. Because of lens curvature, objects approaching the edges of the optical FOV or moving out of the central focal plane may appear distorted, leading to erroneous strain measurements. Lenses corrected for a flat imaging field can reduce these errors. To assess optical strain error in our system we tracked apparent "displacement" and "strain" between two fixed micro-sphere patterns on an acrylic beam that was translated either parallel to the loading axis (20-μm steps) or perpendicular to the imaging plane (5-μm steps) (Figures 2a and 2b). The real strain between patterns on this fixed and rigidly translated object should be zero.

The accuracy of displacement and strain tracking for both large incremental strains across the entire optical FOV and small incremental strains at the typical optical gauge length [~3.0-mm] were quantified by measuring apparent "displacement" and "strain" between micro-sphere patterns on two fluorescently labeled acrylic beams that were translated toward each other (Figures 2c and 2d). Separation of the label patterns was maximized within the FOV to obtain a baseline inter-pattern length (L_o = ~3.0-mm). The actuator was then used to translate one labeled beam toward the other in either +20-mm or ±2-mm steps (Figures 2c and 2d). Displacement and strain were measured optically at each incremental position and compared to values derived from the actuator's linear variable differential transducer (LVDT).

Strain Measurement in Various Materials

To validate the measurement technique's applicability for determining elastic or Young's moduli, deformation and strain were quantified in beams machined from well-characterized synthetic and biological materials (Figure 3a). Acrylic and ultra high molecular weight polyethylene (UHWPE) (McMaster-Carr, Robbinsville, NJ), and intact bovine femora (obtained from a local butcher) were cut into 2×2×25-mm and 1×1×25-mm beams, respectively, using a low-speed saw and diamond-coated wafering blades (Buehler, Lake Bluff, IL). Bovine bone beams were cut from the femoral mid-diaphyseal cortex with the long axis of the beam paralleling the longitudinal axis of the bone shaft. The cross-section of all beams was measured using a digital caliper. The two ends of each beam were embedded in square brass tubes (4.75×4.75×10-mm, McMaster-Carr) using a fast curing acrylic adhesive (Scotch-Weld DP810, 3M, St. Paul, MN) and allowed to cure at room temperature until hard (~6 to 12-hours) (20). To prevent drying, bovine bones were potted, labeled, and tested under conditions of 100% humidity. Fluorescent micro-spheres were adhered to the beams as describe above and the beams were positioned in the loading device with the labeled surface parallel to the imaging plane. Incremental, static, compressive loads up to 8-N were applied to the beam samples (Figure 3a) and strains were quantified optically as described above. Stresses were calculated from the initial cross-sectional areas of the beams. Eight to ten beams were tested for each material. Young's moduli were obtained from the respective stress-strain curves.

Strain Measurement in Murine Tibia

After the accuracy of our strain measurements was established, the system was used to measure local surface strains in intact murine tibiae under uni-axial compressive loads (Figure 3b). This loading configuration will be used for future FRAP flow studies. Right tibiae of six 12-week old male C67BL6/J inbred mice (Jackson Laboratories, Bar Harbor, ME) were harvested,

NIH-PA Author Manuscript

NIH-PA Author Manuscript

NIH-PA Author Manuscript

cleansed of soft tissue, and stored at −40°C in PBS supplemented with 1.4-mM calcium. Prior to testing, tibiae were thawed to room temperature. Micro-spheres were applied to the antero-medial surface of the mid-shaft as described above. Tibiae were positioned in the testing device with the proximal end of the tibia fixed at the reaction bracket and a largely flat anterior-medial surface region was positioned parallel to the imaging plane. Incremental compressive loads, up to 5-N, were then applied through the distal end of the tibia (Figure 3b) and surface strains were measured as described above. Tibiae were tested under conditions of 100% humidity. Our Institutional Animal Care and Use Committee approved all animal procedures.

Statistics

Data are presented as means and standard deviations. Regression analyses were performed using the Prism statistical software package (GraphPad, La Jolla, CA).

Results

System Calibration

Uni-axial strain errors due to in-plane and out-of-plane optical distortions were found to be very small in our system (Figures 4a and 4b). Across the entire FOV displacement and strain errors due to optical distortion averaged −0.37-μm and −144-με; differences between adjacent measures never exceeded 100-με (Figure 4a). Apparent strain due to translation above and below the central focal plane exhibited a parabolic curve (Figure 4b). Vertical shifting of the focal plane by ±150-μm induced an apparent strain less than −200-με.

High accuracy of measurements was demonstrated for both large and small displacement conditions, with optical measures closely agreeing with actuator readings (r^2 value close to 1.0, Figure 4c & 4d). For the 20-μm incremental steps across the FOV optically and actuator derived displacements and strains exhibited maximal difference of 0.61-μm and 400-με, respectively (Figure 4c). For the small displacement tests at 2.0-μm steps the error between the two measures averaged 0.38-μm and 135-με, respectively. Repeated imaging indicated an optical positional accuracy of 0.33-μm, equivalent to 0.25-pixels or ~100-με, for any given translation (data not shown). This accuracy was superior to the positional uncertainty of the actuator (±1-μm or 300-με). Overall, the system exhibited a strain sensitivity of ~200-με for strains up to ±7000-με (i.e., 0.7%) across a gauge length of ~3.0-mm.

Strain Measurement in Various Materials Under Uniaxial Compression

Surface strains, between 0 and 3000-με were measured optically for uni-axially applied compressive loads (0.2 – 8.0-N) in beams of acrylic, UHMWPE, and bovine femoral cortical bone. In all samples a linear relationship between measured strain and applied load (not shown), and stress (Figure 5) was observed. The elastic moduli for the materials tested in our system were consistent with previously reported values, although they are at the lower end of reported values [Table 1].

Strain Measurement in Murine Tibia

Intact murine tibiae with intact articular cartilage were axially compressed at the bone ends. Due to curvature of the tibia, tensile strains were induced on the anterior-medial surface. The relationship between surface strain and applied load at this location was observed to be highly linear (strain [με] = 170.5 *Load [N] − 18.5, $r^2 = 0.87$, $p<0.001$, Figure 6). Because of the bone curvature, the imaged surface was found to have a small out-of-focus shift, which we found to be less than 50-μm under ~5-N peak load during the ~90-second test; the associated strain measurement error was expected to be small (~125-με, Fig. 4b). Horizontal translation of the imaged region was noted due to creeping of the tibiae, however, the translation was relatively

NIH-PA Author Manuscript

NIH-PA Author Manuscript

NIH-PA Author Manuscript

small (~40-μm, or ~2.3% of FOV) during the testing period. No surface rotation or tilting was detected.

Discussion

Quantitative studies of the adaptation of a biological tissue, like bone, to external mechanical loads require accurate quantification of the resultant tissue strains. Many techniques have been developed for strain measurement in biological specimens. However, none of them have permitted parallel strain measurement and live imaging of biological processes in a mechanically loaded bone. To this end, we adopted a simple but powerful optical strain measurement technique and integrated it with a widely used confocal microscope and a linear testing motor. This integrated system will allow us i) to apply well-controlled loads to murine tibiae, ii) to quantify the resultant surface strains, and iii) perform parallel confocal imaging of downstream biological processes, such as load-induced molecular transport and signaling in the same area. We first calibrated the intrinsic system errors due to optic distortion and the accuracy of both large and small displacement tracking. We then tested the system using regular-shaped beams machined from known materials. Finally, we demonstrated the feasibility of using the system on the irregular-shaped murine tibiae.

Our calibration tests indicated minimal systemic errors due to optical distortion and the measurement accuracy was similar to, if not better than, that of the internal actuator positional sensor. With sub-pixel digital image correlation analysis and fine tuning of imaging conditions, in particular, focusing on a relatively flat specimen surface and carefully aligning the loading direction and image plane, accurate quantification of physiologically relevant displacements and strains as low as ~0.65-μm, or ~200-με over a gauge length of ~3.0-mm was ensured. The accuracy of our system was further proven by successfully measuring the elasticity of several materials. The measured material properties agreed with previously reported values (21–25). It is noted that our measures tended toward the lower range of published values. Possible explanations for this include intrinsic differences in material properties between tested specimens, the presence of slight optical aberrations, variability in beam machining, and the potential of specimen creeping. Although significant creeping was not expected during the brief ~5-sec imaging period (26), it might occur over the course of each trial (~60–90-seconds). Greater variability in the strain measures for the less stiff and more plastic UHWMPE, as compared to acrylic and bovine bone (Figure 5) supports the last speculation. Applicability of our extensometry system to small biological samples with complex geometry was demonstrated by measuring surface strains in intact murine tibiae. The observed relationship between surface strains and applied loads was largely consistent with previous strain gauge measurements (~10–25% difference between studies) (12,27). We suspect that these differences may be due to difference in animal ages, measurement locations, or sample preparation/handling methods.

Several limitations were associated with our optical extensometry system. Firstly, although the CCD camera was faster (~2-frame/sec) than the raster scanning of the confocal microscope (~0.25 frame/sec) it was not fast enough to track dynamically applied loads, necessitating the use of static loads in this study. This can be overcome by using higher-speed cameras or confocal microscope such as the Zeiss LIVE system (28,29). Secondly, the strain values reported here were restricted to uni-directional surface measures because these strains in the tibial shaft were found to be the dominant driving force for the load-induced bone fluid flow, the focus of our ongoing studies (7). It is noted, however, that two-dimensional strain tensor measures could be achieved by using a more comprehensive correlation method as demonstrated in previous studies (30). In fact, we tested the feasibility of strain field mapping using a publicly available MATLAB DIC package (http://imechanica.org/node/776) in a small sample sub-set, which also confirmed our uniaxial strain results (data not shown). Thirdly,

NIH-PA Author Manuscript

NIH-PA Author Manuscript

NIH-PA Author Manuscript

because of the small dimensions and possible creeping of our beam samples and intact murine tibiae, we did not use traditional strain gauging or grip-to-grip extensometry techniques to directly validate the optical measurement results. Our results were indirectly validated by the agreement of the derived beam material properties with previously published data (Table 1), and by the general agreement of strain measures of tibiae in other studies (12,27). Lastly, whereas the strain sensitivity of the optical system is less than some conventional methods, such as strain gauging (31), it was adequate for measuring physiologically relevant strain ranging from 200 to ~3000με, and has the benefits of being non-destructive and easily implemented.

The major advantage of the non-contact optical extensometry system described herein is its compatibility with advanced confocal imaging modules, which will allow the study of tissue-level or cellular responses to well-controlled mechanical loads *in situ* and in real time. The extensometry system described here can be applied to a large range of specimens and tissue/material types, including, but not limited to, bone, cartilage, tendon/ligament, muscle, and skin. We are currently using the system to apply physiological strains to murine tibiae and to investigate how mechanical loading influences fluid and solute movement in the bone lacunar-cannicular system (6,7). Quantitative data on these physical processes will help us to understand what mechanical variables are important for triggering the cascade of cellular and biochemical processes involved in the skeletal system's responses to mechanical usage.

Acknowledgments

The authors would like to acknowledge the assistance of Steve Beard (UD Engineering Machine Shop), Laura Shultz, and Scott Prior in developing the loading/imaging system. This research was funded through grants from the National Institutes of Health (P20RR016458; RO1AR054385) and the University of Delaware Research Foundation.

References

1. Cowin SC. Structural changes in living tissues. Meccanica 1999;34(5):379–398. [PubMed: 17672008]
2. Mackey AL, Heinemeier KM, et al. Dynamic adaptation of tendon and muscle connective tissue to mechanical loading. Connect Tissue Res 2008;49(3):165–168. [PubMed: 18661335]
3. Brommer H, Brama PA, et al. Functional adaptation of articular cartilage from birth to maturity under the influence of loading: a biomechanical analysis. Equine Vet J 2005;37(2):148–154. [PubMed: 15779628]
4. McCreadie BR, Hollister SJ. Strain Concentrations Surrounding an Ellipsoid Model of Lacunae and Osteocytes. Comput Methods Biomech Biomed Engin 1997;1(1):61–68. [PubMed: 11264797]
5. Wang Y, McNamara LM, et al. A model for the role of integrins in flow induced mechanotransduction in osteocytes. Proc Natl Acad Sci U S A 2007;104(40):15941–15946. [PubMed: 17895377]
6. Wang L, Wang Y, et al. In situ measurement of solute transport in the bone lacunar-canalicular system. Proc Natl Acad Sci U S A 2005;102(33):11911–11916. [PubMed: 16087872]
7. Zhou X, Novotny JE, et al. Modeling fluorescence recovery after photobleaching in loaded bone: potential applications in measuring fluid and solute transport in the osteocytic lacunar-canalicular system. Ann Biomed Eng 2008;36(12):1961–1977. [PubMed: 18810639]
8. Li W, Novotny JE, et al. The dependency of solute diffusion on molecular weight and shape in intact bone. BONE. 2009 DOI: 10.1016/j.bone.2009.07.076.
9. Silva MJ, Brodt MD, et al. Finite element analysis of the mouse tibia: estimating endocortical strain during three-point bending in SAMP6 osteoporotic mice. Anat Rec A Discov Mol Cell Evol Biol 2005;283(2):380–390. [PubMed: 15747345]
10. Turner CH, Akhter MP, et al. A noninvasive, in vivo model for studying strain adaptive bone modeling. Bone 1991;12(2):73–79. [PubMed: 2064843]
11. Webster DJ, Morley PL, et al. A novel in vivo mouse model for mechanically stimulated bone adaptation--a combined experimental and computational validation study. Comput Methods Biomech Biomed Engin 2008;11(5):435–441. [PubMed: 18612871]

NIH-PA Author Manuscript

NIH-PA Author Manuscript

NIH-PA Author Manuscript

12. Fritton JC, Myers ER, et al. Loading induces site-specific increases in mineral content assessed by microcomputed tomography of the mouse tibia. Bone 2005;36(6):1030–1038. [PubMed: 15878316]
13. Tommasini SM, Morgan TG, et al. Genetic variation in structure-function relationships for the inbred mouse lumbar vertebral body. J Bone Miner Res 2005;20(5):817–827. [PubMed: 15824855]
14. van Lenthe GH, Voide R, et al. Tissue modulus calculated from beam theory is biased by bone size and geometry: implications for the use of three-point bending tests to determine bone tissue modulus. Bone 2008;43(4):717–723. [PubMed: 18639658]
15. Zhang D, Arola DD. Applications of digital image correlation to biological tissues. J Biomed Opt 2004;9(4):691–699. [PubMed: 15250755]
16. Sanghavi P, Bose D, et al. Non-contact strain measurement of biological tissue. Biomed Sci Instrum 2004;40:51–56. [PubMed: 15133934]
17. Derwin KA, Soslowsky LJ, et al. A new optical system for the determination of deformations and strains: calibration characteristics and experimental results. J Biomech 1994;27(10):1277–1285. [PubMed: 7962015]
18. Kim DG, Brunski IB, et al. Microstrain fields for cortical bone in uniaxial tension: optical analysis method. Proc Inst Mech Eng [H] 2005;219(2):119–128.
19. Nicolella DP, Nicholls AE, et al. Machine vision photogrammetry: a technique for measurement of microstructural strain in cortical bone. J Biomech 2001;34(1):135–139. [PubMed: 11425075]
20. Courtland HW, Nasser P, et al. Fourier transform infrared imaging microspectroscopy and tissue-level mechanical testing reveal intraspecies variation in mouse bone mineral and matrix composition. Calcif Tissue Int 2008;83(5):342–353. [PubMed: 18855037]
21. Hoc T, Henry L, et al. Effect of microstructure on the mechanical properties of Haversian cortical bone. Bone 2006;38(4):466–474. [PubMed: 16332459]
22. Martin, RB.; Burr, DB., et al. Skeletal tissue mechanics. New York: Springer; 1998. p. 392pp xiv
23. Cowin, SC. Bone mechanics. Boca Raton, Fla: CTC Press; 1989. p. 313
24. McMaster-Carr. Technical Documents 8574KAC; 8657KAC. 2008. www.mcmaster.com
25. Reilly DT, Burstein AH. Review article. The mechanical properties of cortical bone. J Bone Joint Surg Am 1974;56(5):1001–1022. [PubMed: 4603167]
26. Sasaki N, Nozoe T, et al. Effect of mineral dissolution from bone specimens on the viscoelastic properties of cortical bone. J Biomech 2008;41(16):3511–3514. [PubMed: 18996531]
27. Stadelmann VA, Hocke J, et al. Strain distribution in mice tibia under axial loading. Numerical and experiemental models. Comput Methods Biomech Biomed Engin 2007;10 Supp 1:89–90.
28. Satoh Y, Nishimura T, et al. Application of real-time confocal microscopy for observation of living cells in tissue specimens. Hum Cell 1998;11(4):191–198. [PubMed: 10363156]
29. Adams MC, Salmon WC, et al. A high-speed multispectral spinning-disk confocal microscope system for fluorescent speckle microscopy of living cells. Methods 2003;29(1):29–41. [PubMed: 12543069]
30. Sutton MA, Ke X, et al. Strain field measurements on mouse carotid arteries using microscopic three-dimensional digital image correlation. J Biomed Mater Res A 2008;84(1):178–190. [PubMed: 17607750]
31. Rubin CT, Lanyon LE. Dynamic strain similarity in vertebrates; an alternative to allometric limb bone scaling. J Theor Biol 1984;107(2):321–327. [PubMed: 6717041]

NIH-PA Author Manuscript

NIH-PA Author Manuscript

NIH-PA Author Manuscript

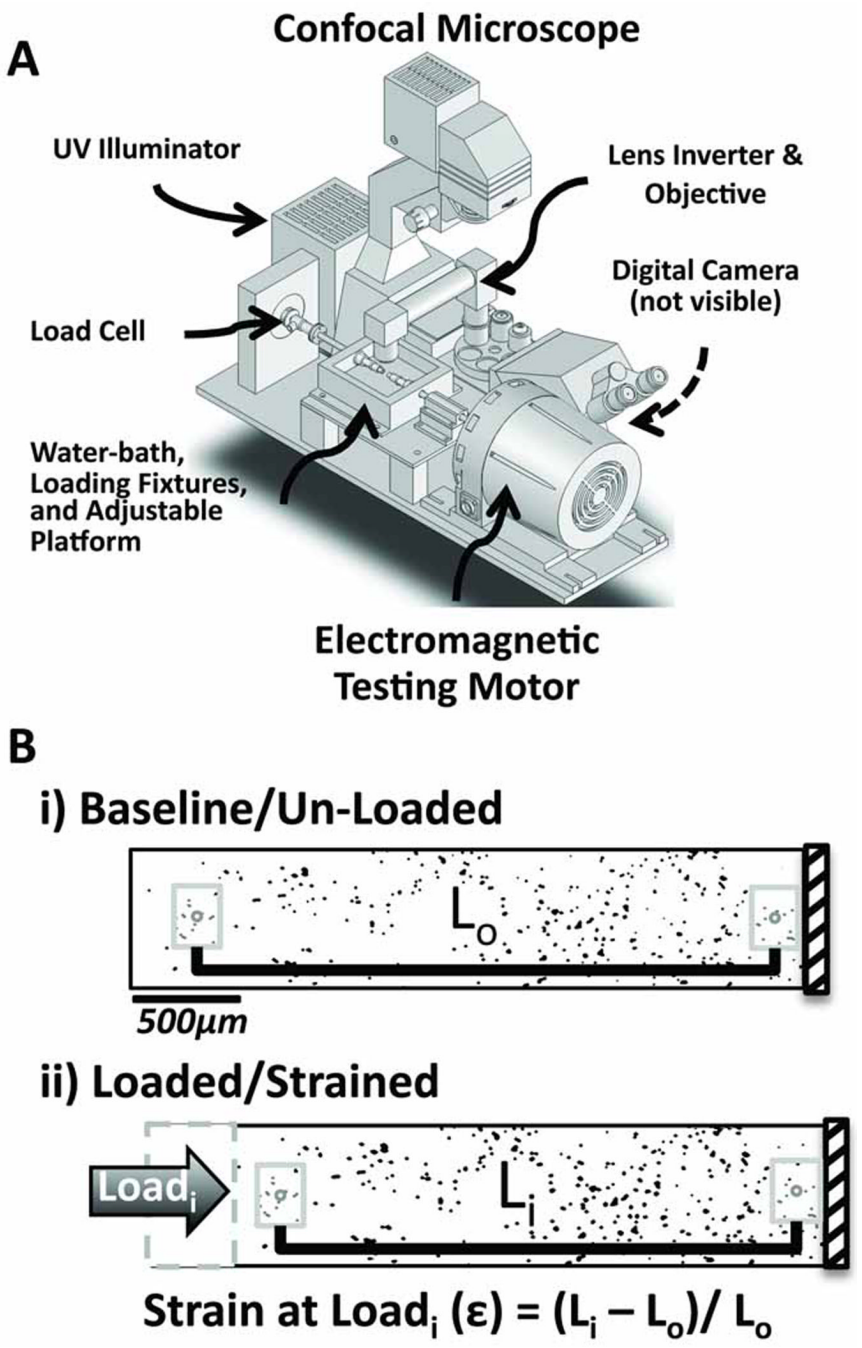

Figure 1.

A) Schematic of the optical extensometry system, consisting of an electromagnetic loading system (Electroforce LM1 TestBench) and a confocal microscope (Zeiss LSM510) with standard epifluorescent imaging capabilities. **B**) Schematic of pattern tracking and strain determination. Fluorescent micro-spheres were used as markers to track strain on the surface of specimens under UV illumination. Unique micro-sphere patterns (shown in grey boxes) were manually selected at the right and left margins of an image and an automated algorithm tracked inter-pattern distance (L_o), displacement (L_i-L_o), and strain (ε) for both baseline and loaded conditions. Displacement and strain are exaggerated for the purpose of illustration.

NIH-PA Author Manuscript

NIH-PA Author Manuscript

NIH-PA Author Manuscript

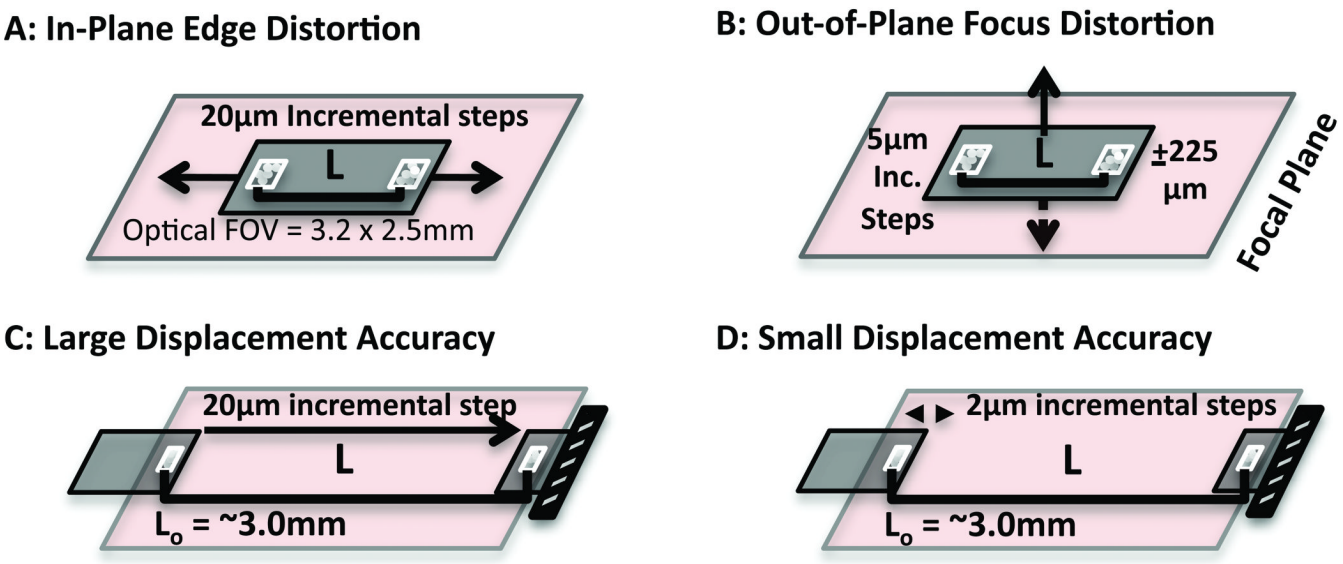

Figure 2.

Four calibration tests to confirm system accuracy. **A**) Apparent strain between fixed micro-sphere patterns due to in-plane edge distortion within the field of view (FOV). **B**) Apparent strain due to out-of-plane focus shifting. **C**) Comparison of the optical and the actuator's positional sensor measures for large (20µm) incremental translations of labeled beams toward each other. **D**) Comparison of the two methods for small (2-µm) incremental translations. An initial gauge length of 3.0-mm was used in C & D. All regressions reported in mm units.

NIH-PA Author Manuscript

NIH-PA Author Manuscript

NIH-PA Author Manuscript

A

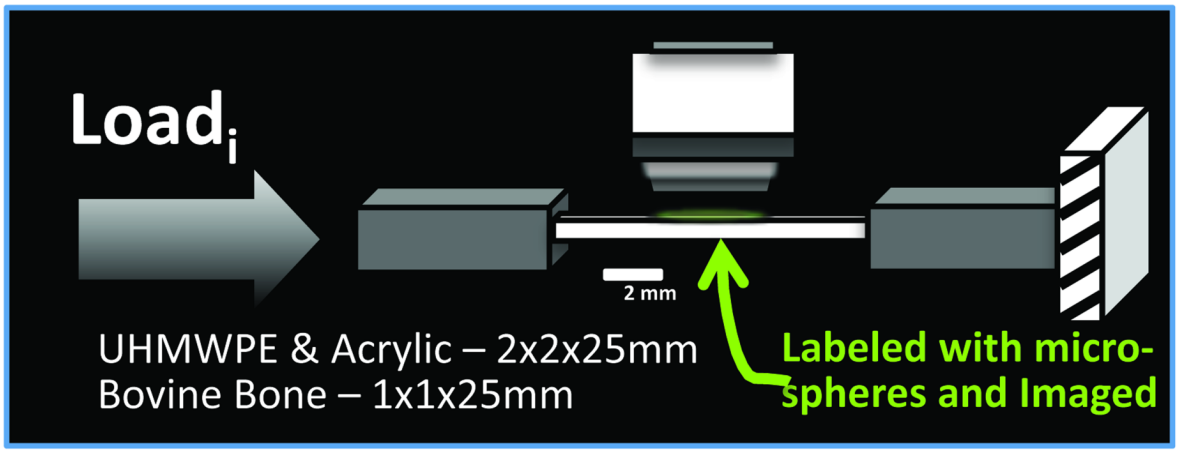

B

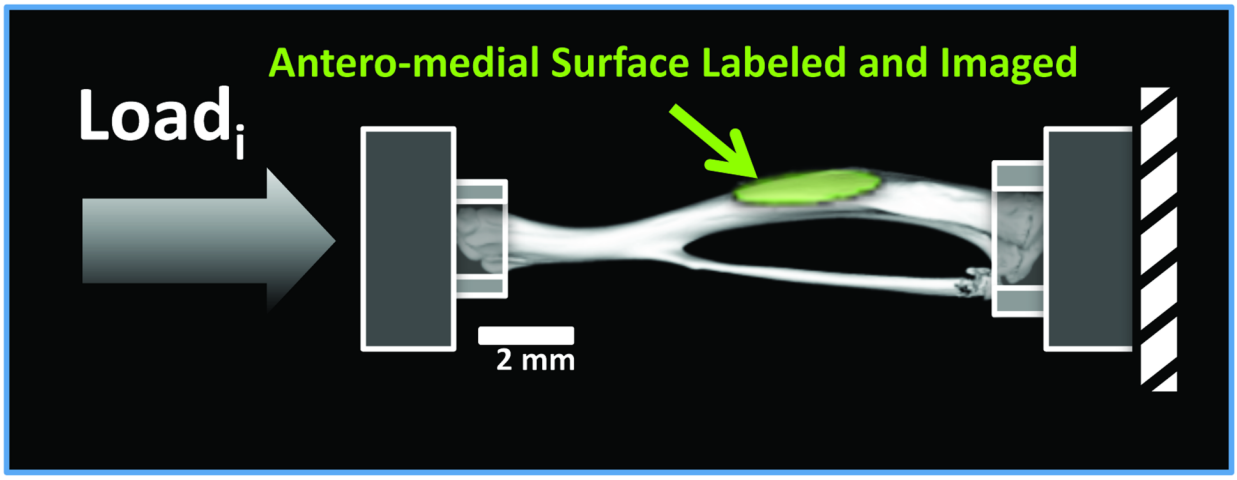

Figure 3.
Schematics of strain measurements location in **A**) machined beams and **B**) murine tibiae under uniaxial compression.

NIH-PA Author Manuscript
NIH-PA Author Manuscript
NIH-PA Author Manuscript

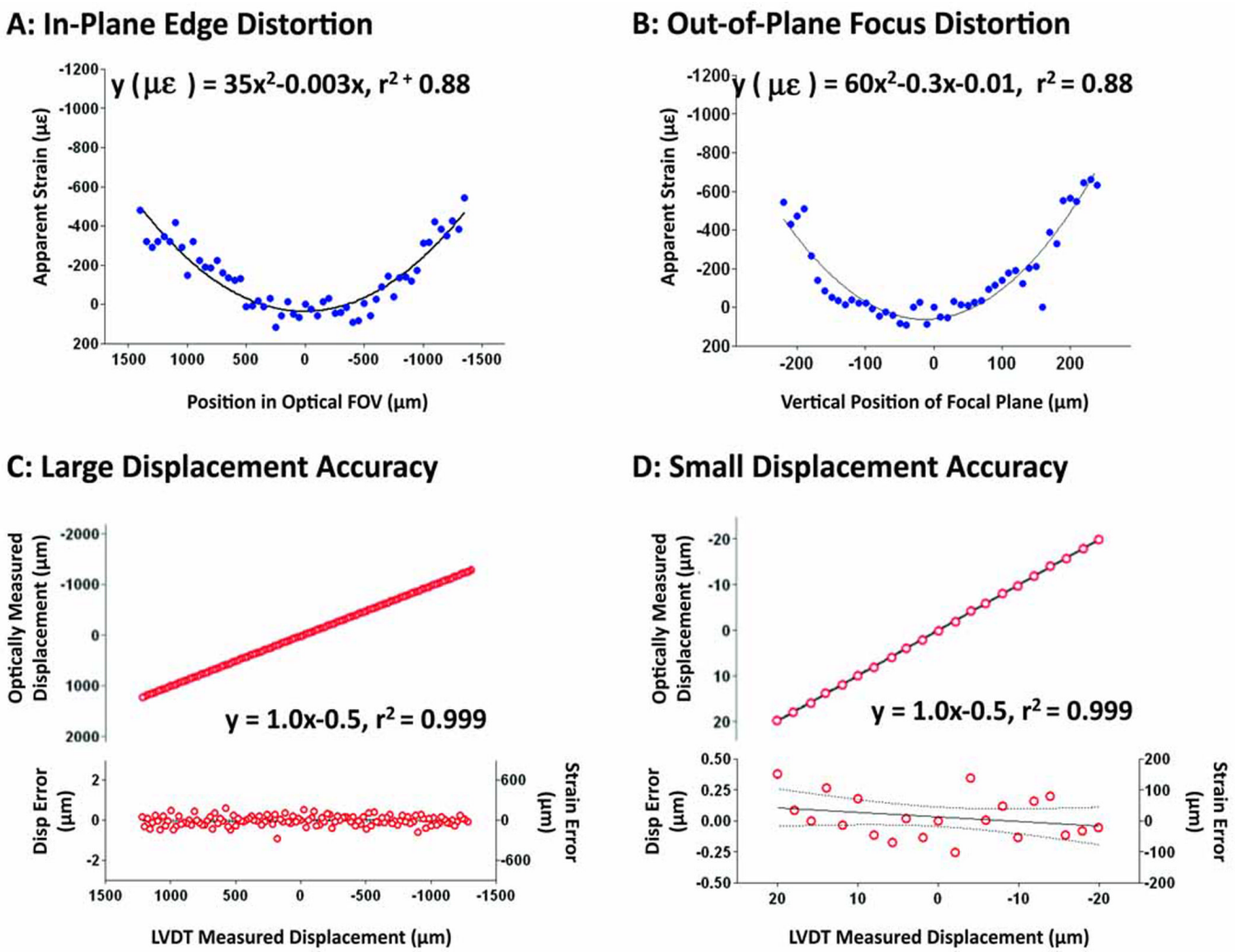

Figure 4.

Minimal errors were found for the optically measured displacement and strain. A) In-plane edge distortion; B) Out-of-plane focus shifting; C) Large displacement tests showed the mean and maximal errors are −0.02 and 0.61-μm, respectively; D) Small displacement tests showed the mean and maximal errors are −0.03 and 0.38-μm, respectively. The initial gauge separation was 3.0-mm for panels C & D. LVDT value of zero corresponds to the center of the camera FOV. Linear regression and 95% confidence intervals are shown.

NIH-PA Author Manuscript
NIH-PA Author Manuscript
NIH-PA Author Manuscript

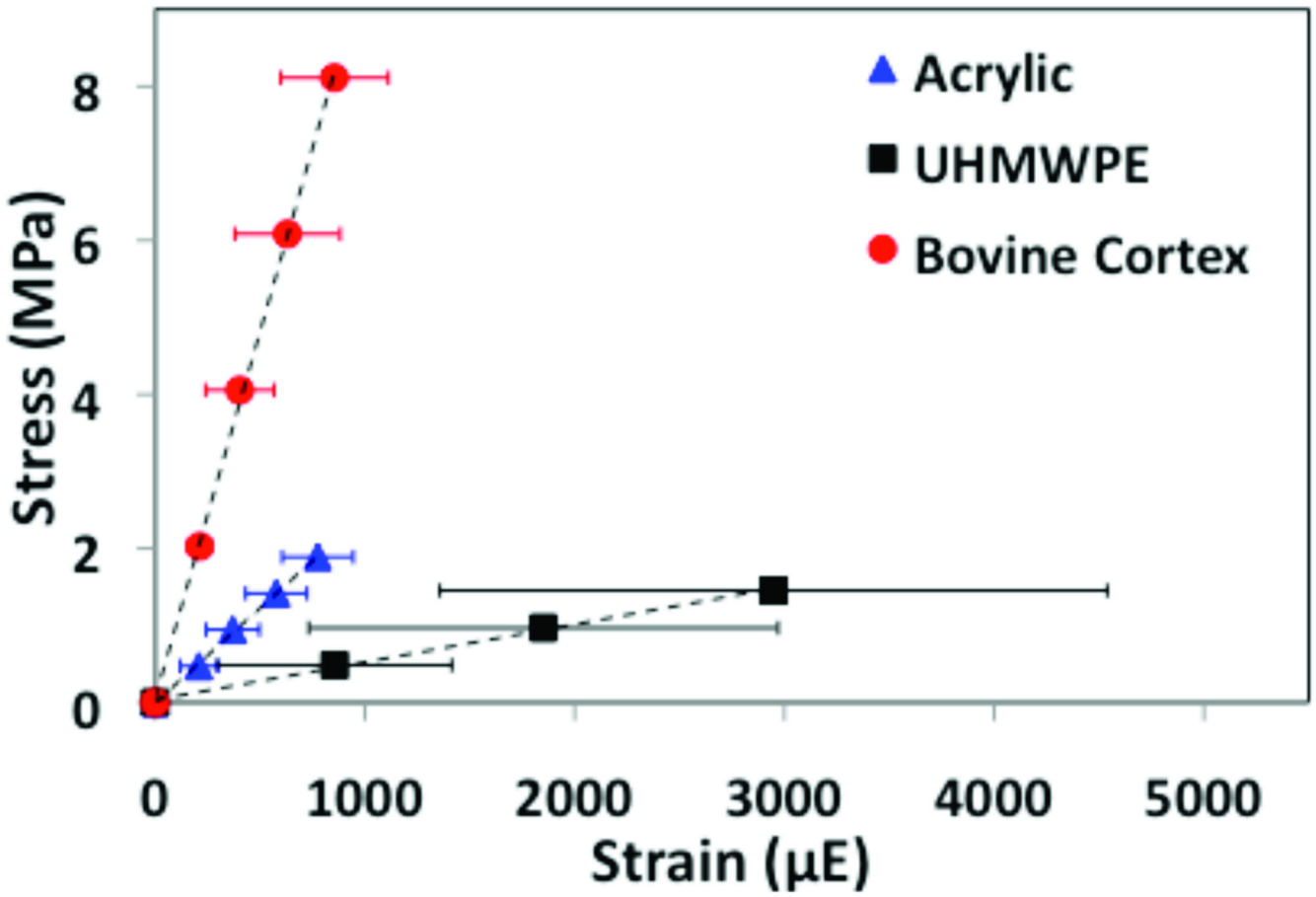

Figure 5.
Stress vs. strain curves for beams machined from UHMWPE, cast acrylic, and bovine femoral cortex (n = 8–10 per material) under uniaxial compression.

NIH-PA Author Manuscript
NIH-PA Author Manuscript
NIH-PA Author Manuscript

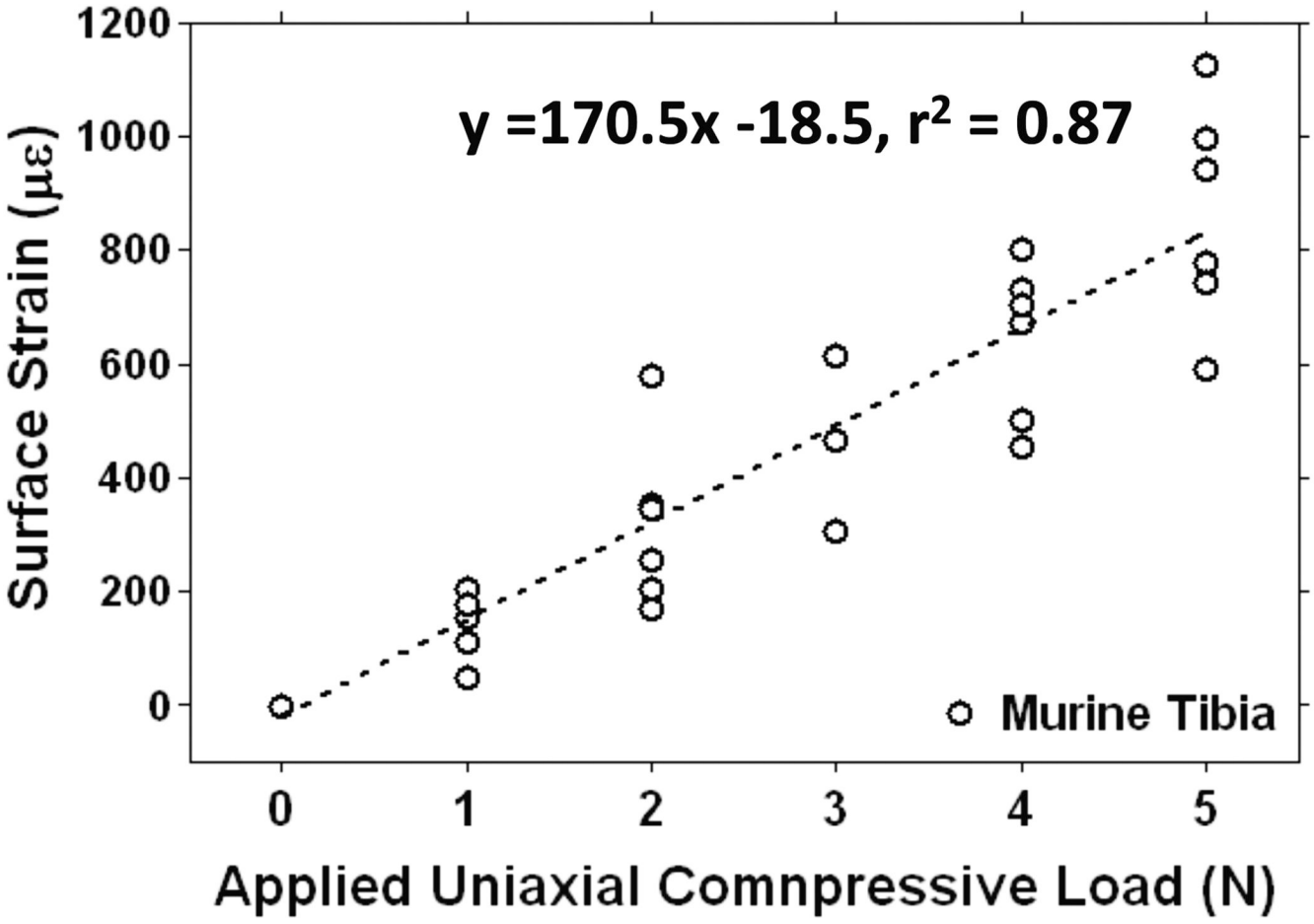

Figure 4.
Strain vs. load curve for adult male B6 mouse tibia under uniaxial compression.

NIH-PA Author Manuscript

NIH-PA Author Manuscript

NIH-PA Author Manuscript

Table 1

Comparison of experimentally derived Young's modulus values (E) for UHWMPE, cast acrylic, and bovine femoral cortex to previously reported values.

Material	Derived Young's Modulus (E)	Previously Reported Young's Modulus (E)
UHMWPE	0.50 ± 0.02 GPa	~0.7 GPa [24]
Cast Acrylic	2.50 ± 0.05 GPa	2.9–3.3 GPa [24]
Bovine Femoral Cortex	9.50 ± 0.17 GPa	9–20 GPa (Macroscopic Moduli 21,22,25) 11–30 GPa (Microscopic moduli 21–23,25)